Inorganic Chemistry

ARTICLE

pubs.acs.org/IC

Syntheses, Crystal Structures, Transport Properties and First-Principles Electronic Structure Study of the $(tTTF)_2X$ (X = Br, I) Low-Dimensional Antiferromagnets

Marc Fourmigué,* Eric W. Reinheimer, Ali Assaf, Olivier Jeannin, and Ali Saad

Sciences Chimiques de Rennes, Université Rennes 1, UMR CNRS 6226, Campus de Beaulieu 35042 Rennes, France

Pascale Auban-Senzier

Laboratoire de Physique des Solides, Université Paris-Sud, UMR CNRS 8502, Bât. 510, 91405 Orsay, France

Pere Alemany*

Departament de Química Física and Institut de Química Teòrica i Computacional (IQTCUB), Universitat de Barcelona, Diagonal 647, 08028 Barcelona, Spain

Antonio Rodríguez-Fortea

Departament de Química Física i Inorgànica, Universitat Rovira i Virgili, Marcel.lí Domingo s/n, 43007 Tarragona, Spain

Enric Canadell*

Institut de Ciència de Materials de Barcelona (CSIC), Campus de la UAB, E-08193 Bellaterra, Spain

Supporting Information

ABSTRACT: An efficient synthetic procedure for the preparation of unsymmetrically substituted tetrathiafulvalene (TTF) donors has been used to obtain the trimethylene-tetrathiafulvalene (tTTF) donor with high purity. Good quality crystals of the two $(tTTF)_2X$ (X = Br, I) salts have been obtained by electrocrystallization. The two salts are isomorphous and contain tTTF layers which are built from $(tTTF)_2$ dimeric units. Both systems are low-dimensional antiferromagnets with the highest Néel temperatures for TTF based radical cation salts: ≈ 35 K (Br salt) and ≈43 K (I salt). The resistivity is found to substantially decrease with pressure although both salts still have activated conductivity at 25 kbar. First-principles Density Functional Theory (DFT) calculations have been used to investigate the relative strength of the three different types of magnetic interactions in the tTTF layers as well as the potential magnetic ground states. These calculations successfully predict the nature of the ground state and suggest a possible correlation between structural details and Néel temperatures for the bromine and iodine salts. Remarkably, the calculated antiferromagnetic ground state can be predicted from the nesting properties of the Fermi surface for the hypothetical Pauli paramagnetic metallic state.

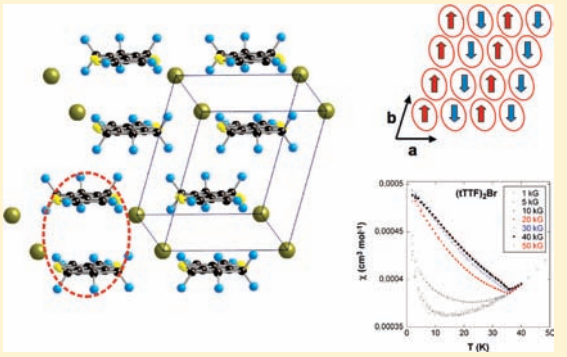

INTRODUCTION

Low-dimensional tetrathiafulvalene (TTF)-based charge transfer molecular solids have led to an apparently never ending list of intriguing discoveries. The relatively small values of both the transfer integrals (t) and the on-site Coulomb repulsions (U) result with complex phase diagrams with several competing ground states (charge or spin density wave, superconducting, charge ordered, metallic, Mott insulating, etc.). For small t/U values, localized spins are created in the π-system of the TTF-based molecular units favoring an antiparallel spin arrangement between adjacent molecules, thus leading to one-dimensional (1D) or two-dimensional (2D) Heisenberg antiferromagnets. Depending on the structural subtleties of the TTF-based lattices,

Received: February 11, 2011
Published: March 29, 2011

these molecular salts exhibit interesting and sometimes competing features like spin-Peierls instabilities, spin frustration, 1D or quasi-2D antiferromagnetic (AF) behavior, and so forth.[1]

Looking for such cation radical salts with an AF ground state, we were attracted by a salt of the unsymmetrically substituted trimethylene-tetrathiafulvalene[2] (noted tTTF) with the bromide anion, that is, $(tTTF)_2Br$, where a Néel temperature of 33 K was reported from electron paramagnetic resonance (EPR) characterizations.[3,4] This temperature is, to our knowledge, the highest one among cation radical salts derived from TTFs and indicates a strong stability of this ordered magnetic phase. Only a few salts have been described so far with tTTF, prepared either by electrocrystallization with small anions (ClO_4^-, ReO_4^-, PF_6^-, AsF_6^-, SbF_6^-) or by chemical oxidation with TCNQ.[5] However, the crystal structure of the bromide salt was unknown, because of the low quality of the crystals obtained then. We report here a high yield synthesis of pure tTTF, its electrocrystallization to the mixed-valence bromide and to the unknown chloride and iodide salts, together with their transport and magnetic properties. The AF ground state observed in a relatively high temperature range in both bromide and iodide compounds is analyzed through first-principles density functional theory (DFT) calculations.

Indeed, in recent years, it has been increasingly clear that modern DFT approaches are reliable enough to accurately describe the electronic structure of low-dimensional molecular metals based on TTF and related systems. Both charge-transfer molecular salts and single-molecule metals have been successfully studied.[6−11] In contrast, not many first-principles band structure studies have been carried out on *localized* TTF-based molecular conductors. Only a very few localized molecular conductors based on transition-metal dithiolate and trithiolate systems have been studied at the DFT level.[12−14] However, to the best of our knowledge, no TTF-based localized molecular salt has been considered through a first-principles DFT approach. This is even more surprising since we have recently shown that these calculations can successfully rationalize the change from a localized semiconductor to a metallic state under pressure for a gold dithiolene complex molecular conductor.[15] Besides their inherent interest, the present tTTF salts thus provide appropriate ground for testing the performance of first-principles DFT calculations for TTF-based localized molecular salts. As it will be shown below, these calculations provide a clear description of the ground state of the two bromide and iodide tTTF salts.

RESULTS AND DISCUSSION

Synthesis and Crystal Growth. As recently reviewed,[16] the preparation of unsymmetrically substituted TTFs often causes difficulties as the main TTF syntheses are based on the symmetrical coupling of two identical halves. The first reported syntheses of the unsymmetrically substituted tTTF molecule involved indeed the statistical cross coupling of the dithiolium and trimethylene-dithiolium cations in the presence of NEt_3, affording a complex mixture of the three possible TTFs, that is, TTF, HMTTF (hexamethylenetetrathiafulvalene), and tTTF, to be tediously separated by chromatography in 25% yield.[17] Following the first report by Gonella and Cava,[18] Fabre et al. investigated in more details a more selective Wittig-type coupling,[19] which was shown to also afford small quantities of the symmetrical TTFs besides tTTF (in 15% yield only), hence limiting the purity and quality of the crystals obtained by electrocrystallization. We have developed over the years[20,21] a fully selective cross coupling reaction

Scheme 1. Synthetic Path to tTTF

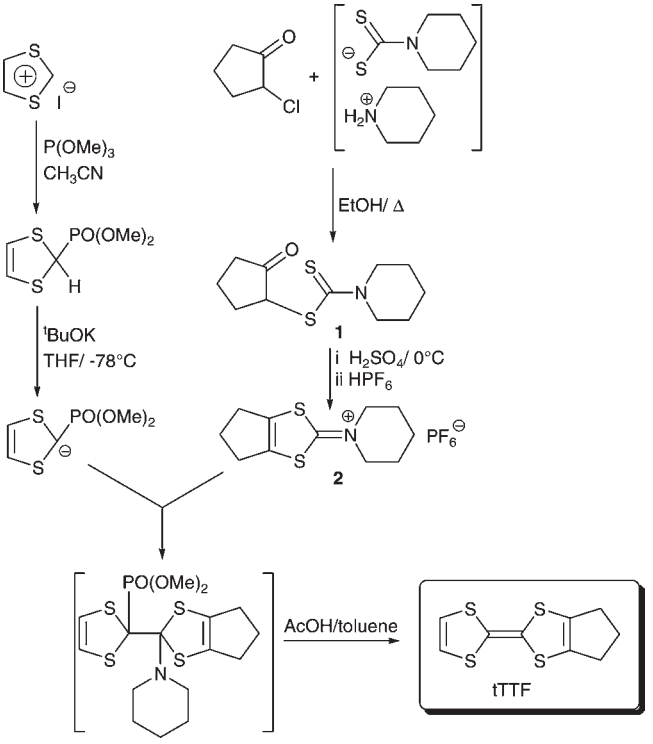

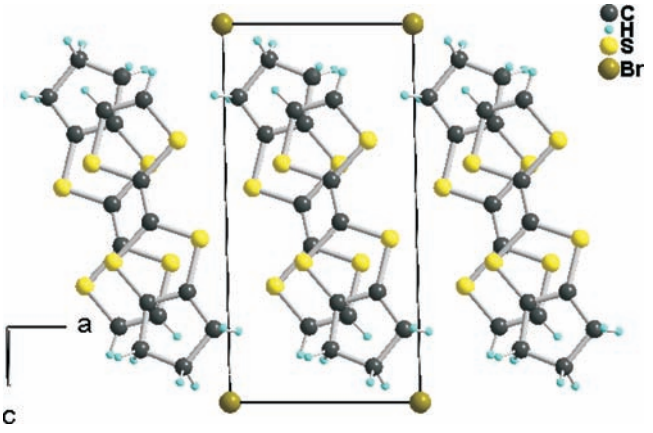

Figure 1. Projection view along the stacking axis *b* of the unit cell of $(tTTF)_2Br$.

toward unsymmetrically substituted TTFs which is based on a Horner−Wadsworth−Emmons reaction (Scheme 1) involving phosphonates as nucleophile precursor and imminium salts as electrophile.[22] Both starting materials are stable in the reaction conditions and do not afford any symmetrical TTFs. Following this route, tTTF was prepared in pure form and in 46% yield, without need for tedious chromatographic separations.

This high purity, combined with the use of EtOH as solvent rather than CH_2Cl_2 or 1,1,2-trichloroethane, allowed for the successful electrocrystallization of the halide salts with good quality crystals with Br^- and I^- while a different phase was obtained with Cl^- in the form of much smaller crystals (see below). Since the first oxidation potential of tTTF is rather low (E°_1 = 0.33 V vs SCE, in CH_2Cl_2), the iodide salt was also obtained in larger

dx.doi.org/10.1021/ic2002964 |*Inorg. Chem.* 2011, 50, 4171–4181

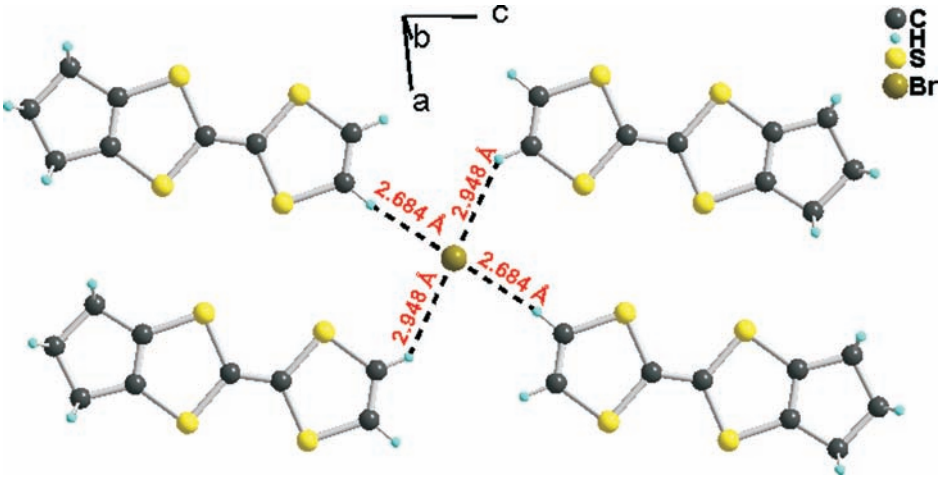

Figure 2. Detail of the C−H···Br^- interactions in $(tTTF)_2Br$.

Table 1. Structural Characteristics of the C−H···X Hydrogen Bonds

	H···X (Å)	C(−H)···X	C−H···X (deg)
		$(tTTF)_2Br$	
C1−H1···Br^-	2.95	3.673(5)	135.9
C2−H2···Br^-	2.68	3.592(5)	165.7
		$(tTTF)_2I$	
C1−H1···I^-	3.13	3.876(2)	138.0
C2−H2···I^-	2.88	3.786(2)	163.7

quantities by diffusion techniques using chemical oxidation with the I_3^- triiodide anion.

Crystal Structure. The chloride salt was obtained only with difficulty and in small quantities. It crystallizes in the monoclinic system, space group $P2_1$ with four crystallographically independent molecules in the unit cell together with two chloride anions. The molecules are associated into trimeric units, separated from each other by a less oxidized molecule. This salt will not be further discussed here (See Supporting Information for more details).

Bromide and iodide salts are isomorphous, they crystallize in the triclinic system, space group $P\bar{1}$, with one tTTF molecule in general position and one halide anion on inversion center. The molecules stack on top of each other along the *b* axis, interacting sideways along *a* (Figure 1).

At variance with most TTF cation radical salts which involve larger counterions, the organic−inorganic interface is limited here to contacts with the Br^- or I^- anions. The environment of the anions is shown in Figure 2 for $(tTTF)_2Br$. It is characterized with two particularly short C−H···Br^- interactions and two others which coordinate the halide anion in a pseudo square-planar environment (Table 1). Such C−H···Hal^- interactions, albeit weak in essence, have been shown to play a crucial role to direct the formation of specific structural patterns in the solid state.[23] In the realm of molecular conductors,[24] they were identified as important structural tools, for example, in TTF·Chloranil[25] charge transfer salt or in various TTF cation radical salts.[21,26,27] However, while the role of chloride anion as H bond acceptor with C−H donors is well documented,[28] it is not the case with bromide or iodide anions.[21,27] A crude approach based on the sum of van der Waals radii confirms the existence of these interactions,

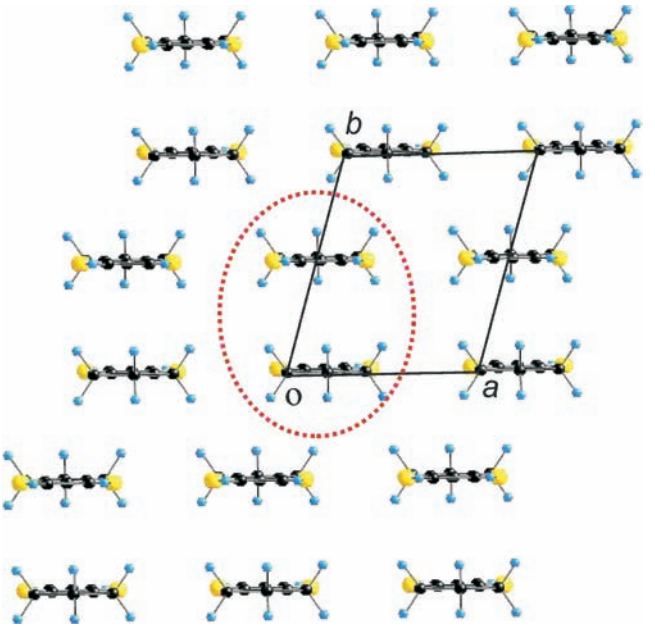

Figure 3. Projection view of one conducting slab in $(tTTF)_2Br$ along the long molecular axis of the donors.

with $\Sigma_{vdW}(H\cdots Br) = 1.20 + 1.85 = 3.05$ Å and for $\Sigma_{vdW}(H\cdots I) = 1.20 + 1.98 = 3.18$ Å, to be compared with the shortest intermolecular distances (H···Br^- = 2.68 Å and H···I^- = 2.88 Å) which are also the most linear ones (C−H···X^- = 164−166°).

It should be stressed at this point that the Br^- and I^- salts are not isostructural with the other salts described so far with tTTF, either with tetrahedral ClO_4^- or BF_4^- (triclinic, association into tetramers),[3,4] or with PF_6^- (monoclinic, $P2_1/n$, solvent inclusion),[4] while they are related to the AsF_6^- and SbF_6^- salts[3,4] which also exhibit an AF ground state below $T_{Néel} \approx 25$ and 19 K respectively. This variability contrasts strongly with the isostructural character of the whole series of TMTTF or TMTSF salts, the so-called Bechgaard salts, where the very same triclinic recurrent structure is systematically observed, whatever the nature of the counterion, be it spherical (Br^-), linear (SCN^-), planar (NO_3^-), tetrahedral (ClO_4^-, ReO_4^-, FSO_3^-, BF_4^-), or octahedral (PF_6^-, AsF_6^-, SbF_6^-).[29]

dx.doi.org/10.1021/ic2002964 |*Inorg. Chem.* 2011, 50, 4171–4181

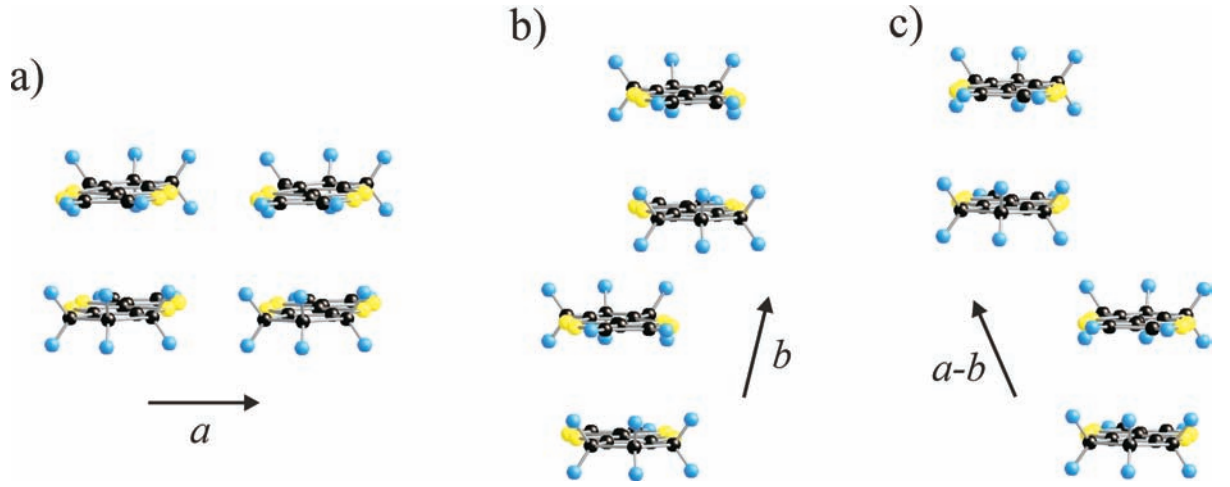

Figure 4. Three different types of interdimer interactions in the tTTF slabs of $(tTTF)_2Br$: along the *a* direction (a), along the *b* direction (b), and along the $a - b$ direction (c).

Table 2. Short S···S Contacts (Å) Associated with the Three Different Interdimer Interactions in the $(tTTF)_2X$ (X = Br, I) Salts

interaction along	$(tTTF)_2Br$	$(tTTF)_2I$
a	3.566, 3.588, 3.593	3.590, 3.617, 3.655
b	3.642 (×2)	3.678 (×2)
$a - b$	3.965 (×2)	3.904 (×2)

Dimer−Dimer Interactions. The structural organization of the partially oxidized tTTF molecules within a conducting slab is shown in Figure 3. It is clear that the structural building blocks of these slabs are inversion-centered $(tTTF)_2$ dimeric units. Within these layers there are three different types of interactions between dimers: those along *a*, along *b*, and along $(a - b)$ (see Figure 4). The interactions between highest occupied molecular orbitals (HOMOs) along *a* are of the π type whereas those along both *b* and $(a - b)$ are fundamentally of σ type. Since the dimerization is quite strong (the overlap is of the ring-over-bond type with four S···S short contacts of 3.593 Å (×2) and 3.611 Å (×2) for the Br salt and 3.595 Å (×2) and 3.597 Å (×2) for the I salt and large intradimer transfer integrals of 0.375 eV for the Br salt and 0.412 eV for the I salt), the appropriate orbital to evaluate the strength of the interactions along the layer is the antibonding combination of the two HOMOs of the dimer (ψ_+). A simple evaluation of the effective transfer integrals associated with ψ_+ using the extended Hückel approach leads to the following values: $t_a = -90$ meV, $t_b = +9$ meV, and $t_{a-b} = +64$ meV. The small value of t_b is due to the lateral sliding of the two interacting donors causing the almost cancellation of the overlaps of the S p_z orbitals of one donor with those of the S and C of the other donor which enter with opposite sign in the tTTF HOMO.

It is clear that the interactions along the direction of the stacks (*b*) are very weak compared with those along the interstack interactions (*a* and $a-b$). Note that those along *a* dominate and are of opposite sign with respect to those along $a - b$. This can be easily understood because they both implicate p_z orbitals but whereas the interactions along *a* are of the π type, those along $a - b$ are mostly of the σ type. In addition, although the π type interactions are generally weaker than the σ ones, in the present case every dimer unit makes two π type interactions along *a* but only one σ type along $a - b$ and finally t_a is the largest one. The short S···S contacts associated with each interaction are reported in Table 2.

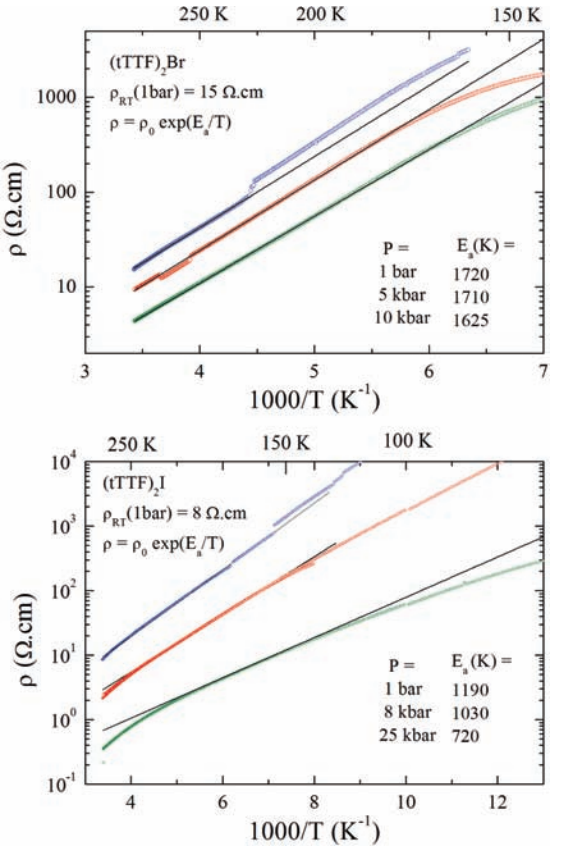

Figure 5. Temperature dependence of the resistivity of $(tTTF)_2Br$ (top) and $(tTTF)_2I$ (bottom) at different applied pressures, plotted as ρ versus the inverse temperature to determine the activation energy E_a. Blue points, 1 bar; red points, 8 kbar, green points, 25 kbar.

Transport and Magnetic Properties. The room temperature resistivity of both salts is essentially the same, varying from 8 to

dx.doi.org/10.1021/ic2002964 |*Inorg. Chem.* 2011, 50, 4171–4181

20 Ω cm depending on the sample. As shown in Figure 5, both salts behave as semiconductors below room temperature. The activation energies E_a evaluated from the relation $\rho = \rho_0 \exp(E_a/T)$ are, at ambient pressure, 1720 K (0.148 eV) in $(tTTF)_2Br$ and 1190 K (0.103 eV) in $(tTTF)_2I$.

The pressure dependence of the room temperature conductivity (Figure 6) shows a faster variation than in nearly metallic $(TM)_2X$ where $\sigma(P)$ is linear with a slope $\Delta\sigma(P)/\sigma(1\ bar) = +20-30\%$/kbar. However, despite this strong decrease of the resistivity under pressure, its temperature dependence is still activated with a small decrease of the activation energy only at 25 kbar (Figure 5). This is the sign that interchain couplings are not significantly increased with pressure.

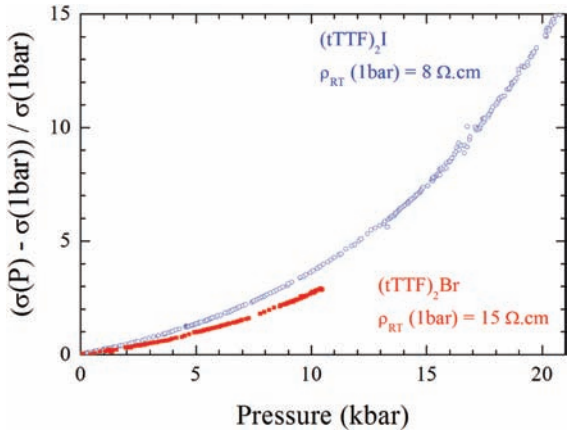

Figure 6. Pressure dependence of the relative increase of conductivity at room temperature for $(tTTF)_2Br$ and $(tTTF)_2I$.

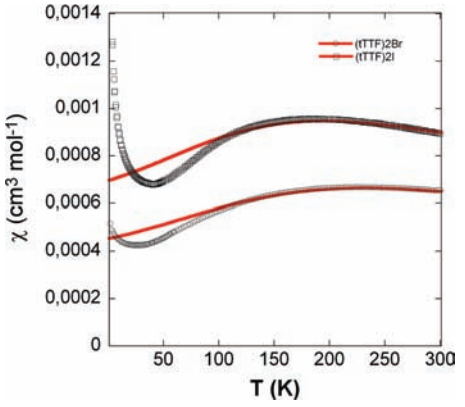

Figure 7. Temperature dependence of the magnetic susceptibility in $(tTTF)_2Br$ and $(tTTF)_2I$. The red line is a fit to the uniform spin chain model (see text).

The temperature dependence of the magnetic susceptibility of both salts is shown in Figure 7. The susceptibility goes through a rounded maximum, indicating the presence of dominating AF interactions in a nonmetallic state. On the basis of the X-ray crystal structure described above, we successfully applied a fit with a uniform spin chain model (Bonner−Fischer)[30,31] with the Hamiltonian $H = -J\sum_{i=1}^{n=1} S_iS_{i+1}$ in the high temperature region ($T > 75$ K), giving J/k values of −350 and −295 K for the Br^- and I^- salt, respectively, together with different temperature independent paramagnetism (TIP) of 4.4(6) 10^{-5} and 20.9(5) 10^{-5} cm^3 mol^{-1} for the Br^- and I^- salt, respectively. At lower temperatures (Figure 8), a strong field dependence characteristic of an AF ground state is observed for both salts, partially blurred in the iodide salt because of the added contribution of paramagnetic impurities (Curie tail). These data confirm the AF ground state in $(tTTF)_2Br$ at a Néel temperature $T_{Néel}(Br) \approx 35$ K with a slightly higher value for the iodide salt, $T_{Néel}(I) \approx 43$ K.

The transport and magnetic properties described above together with the half-filled band character allow us to describe these salts as Mott insulators with higher activation energies than in the $(TM)_2X$ salts. Moreover, the 1D character is maintained under high pressure so that the Mott insulator-metal transition is not reached.

Hypothetical Pauli Paramagnetic Metallic State. Even if the system is localized, it will be useful to begin the analysis of the electronic structure of these salts by looking at their hypothetical Pauli paramagnetic metallic state. Except otherwise stated, all results reported from now on are those for the Br salt (those for the I salt are very similar). The band structure near the Fermi level for the metallic state calculated without spin-polarization is shown in Figure 9a. The two bands in this figure are almost exclusively built from the HOMO of tTTF, and the average energies of the two bands are separated by approximately 0.5 eV, as it corresponds to a dimerized system. Since there is one hole per dimer, the upper band is half filled. This band exhibits a quite sizable dispersion, ~0.35 eV, suggesting substantial interaction between dimers. The shape of this partially filled band can be easily explained by taking into account the interdimer transfer integrals discussed above, as well as the phase factors associated with the different *k*-points.

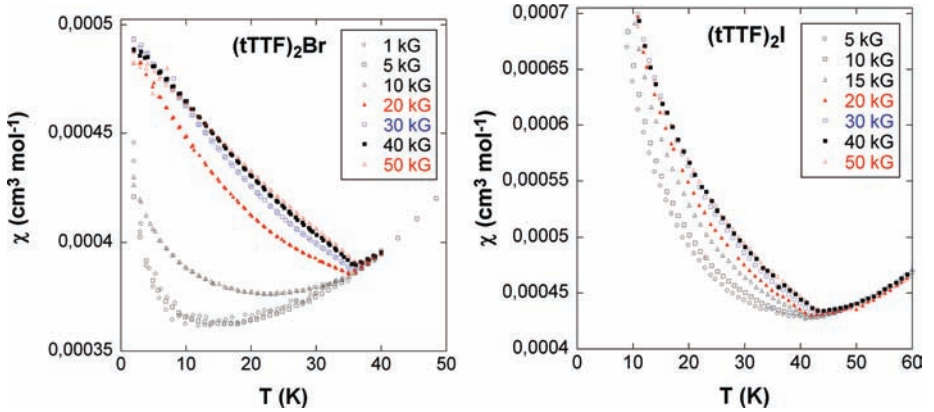

Figure 8. Temperature and field dependence of the magnetic susceptibility in $(tTTF)_2Br$ and $(tTTF)_2I$ at lower temperatures.

dx.doi.org/10.1021/ic2002964 |Inorg. Chem. 2011, 50, 4171–4181

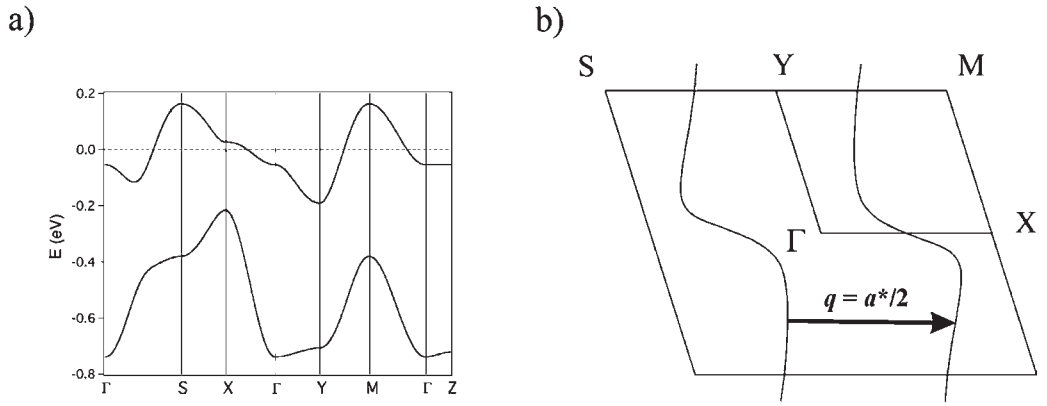

Figure 9. Calculated (a) band structure and (b) Fermi surface for the Pauli paramagnetic metallic state of $(tTTF)_2Br$. The dashed line in (a) refers to the Fermi level and Γ = (0, 0, 0), X = (1/2, 0, 0), Y = (0, 1/2, 0), Z = (0, 0, 1/2), M = (1/2, 1/2, 0), and S = (−1/2, 1/2, 0) in units of the triclinic reciprocal lattice vectors.

Table 3. Calculated Magnetic Coupling Constants (in K) for the Three Different Directions of the Lattices of the $(tTTF)_2X$ (X = Br, I) Salts

interaction	$(tTTF)_2Br$	$(tTTF)_2I$
J_a	−164	−150
J_b	−0.5	+0.2
J_{a-b}	−31.8	−47.7

The associated Fermi surface is shown in Figure 9b and is made of two warped lines. In agreement with the analysis of the dimer−dimer interactions, it corresponds to a pseudo-1D system along the *a* direction. Note that this is not the stacking direction. As it will be shown later, an important observation is that this Fermi surface is very well nested by the vector $q = a^*/2$. This feature suggests that since the electron repulsions in this system must be very significant, there may be a substantial energy gain if there is a doubling of the periodicity in the spin degrees of freedom along the *a* direction. Note that because of the nature of the lattice, a doubling along *a* necessarily means also a doubling along $(a - b)$ if there is no change along *b*.

Magnetic Interactions between Dimer Units. Before proceeding to verify the previous suggestion, we need to have some hint concerning the strength of the three different types of magnetic coupling constants in the lattice. A simple way to do it is by carrying out calculations for the interaction of two dimeric units with exactly the same geometry that they have in the solid. From the energy difference between the associated singlet and triplet states, the different *J* coupling constants can be evaluated (see Table 3). Thus, the interactions along *a* are calculated to be strongly AF, those along $(a - b)$ are moderately AF, and those along *b* are practically nil. These values are fully consistent with the possibility highlighted by the analysis of the Fermi surface. Note that these coupling constants are not directly comparable to those discussed above which were obtained by fitting the data to a uniform spin chain model.

Stability of Different States. Let us now consider the stability of different states for $(tTTF)_2Br$ using spin-polarized calculations. We first considered the case of a ferromagnetic state. We obtained a state which is 27.2 K per formula unit more stable than the Pauli paramagnetic metal. However, when looking at the band structure of the system (see Figure 10) it is clear that the upper spin-up (full line) and spin-down (broken line) bands overlap so that this state is not an insulating ferromagnetic state but a ferromagnetic metal.

With this band structure it is clear that the total spin per tTTF molecule must be lower than +1/2 because of the itinerant part. The calculated spin density is shown in Figure 10b, and the total spin density per tTTF is calculated to be only +0.122, which means that the system has a large itinerant part. What these results illustrate is that introduction of ferromagnetic type interactions stabilize the system while keeping the metallic character. The next step is to consider how the introduction of AF interactions changes the stability of the system. Given the nature of the layers there are three different ways to introduce AF interactions (see Figure 11).

Introduction of AF interactions along both *a* and *b* necessarily leads to the introduction of ferromagnetic interactions along $a - b$ (state AF in Figure 11); introduction of AF interactions along *a* necessarily leads to the introduction of AF interactions along $a - b$ if the interactions along *b* are ferromagnetic (state AFa in Figure 11); finally, introduction of AF interactions along *b* necessarily leads to the introduction of AF interactions along $a - b$ if there are ferromagnetic interactions along *a* (state AFb in Figure 11). We have calculated the stability of these states and found the results of Table 4. In view of these results we can conclude that introduction of AF type interactions is more effective than introducing ferromagnetic type interactions in stabilizing the system.

The relative stability of the three AF states is easily understood when the approximate *J* values of Table 3 are taken into account. Consequently, it appears that introducing AF interactions along *a* clearly leads to the ground state of the system. However, before comparing with the experimental situation, we must consider if these AF states are genuine (i.e., semiconducting) AF states or not. The calculated band structures for the three states are shown in Figure 12. Those for AFb and AF *do not* exhibit a band gap and consequently are AF metals.[32] In contrast, AFa, the most stable state calculated for $(tTTF)_2Br$ is a genuine semiconducting antiferromagnet. This has been verified by plotting the separate spin-up and spin-down densities of states for every dimer and verifying that the contributions of two adjacent dimers along *a* and $a - b$ are identical but opposite in sign. Thus, we conclude that the ground state for $(tTTF)_2Br$ must be a semiconducting AF state, in agreement with the transport measurements. It is worthwhile noting that the type of spin ordering in AFa is possible because of the almost nil magnetic interactions along the *b* direction.

dx.doi.org/10.1021/ic2002964 |*Inorg. Chem.* 2011, 50, 4171–4181

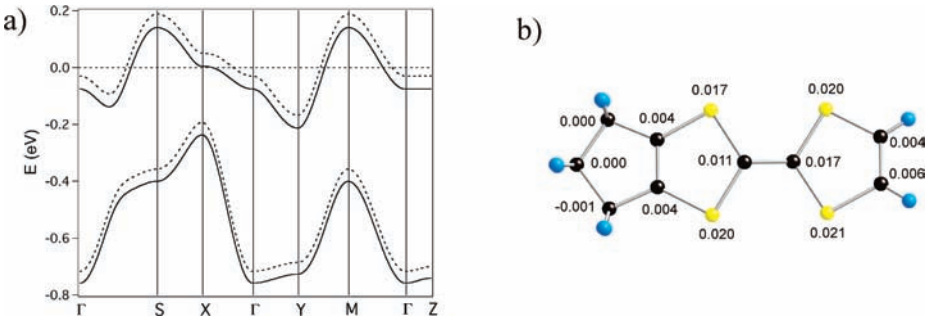

Figure 10. (a) Band structure (HOMO bands) for the calculated ferromagnetic state of $(tTTF)_2Br$ (spin-up bands: full lines; spin-down bands: broken lines). Since the two upper bands overlap the system is a ferromagnetic metal, and the Fermi level is indicated by the dashed line. (b) Calculated spin density distribution for this state.

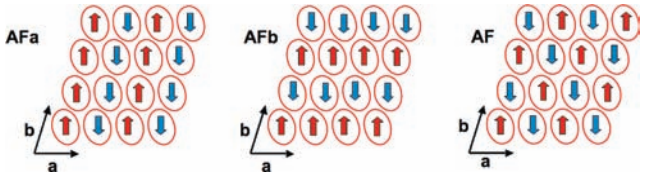

Figure 11. Schematic representation and labeling of the different AF states considered.

Table 4. Relative Stability of the Different States Calculated for $(tTTF)_2Br$[a]

state	relative energy
Pauli paramagnetic metal	0.0
FM	−25.5
AFb	−40.8
AF	−49.3
AFa	−98.7

[a] In K per formula unit.

Had this magnetic interaction been larger, a complex spin ordering due to partial spin frustration could have occurred. It is remarkable that the weakness of the magnetic interaction along the *b* direction is associated with relatively short S···S contacts. However, the overlap mode between the dimeric units, with a strong lateral displacement, is associated with a very small overlap and coupling constant.

The calculated spin densities at each site of the tTTF donors for the FM, AFa, AFb, and AF states are shown in Figure 13. The total spin densities per tTTF donor are calculated to be 0.122 (FM), 0.167 (AFb), 0.198 (AF), and 0.322 (AFa). The three correlated metals have relatively similar and quite low spin densities whereas for the semiconducting AF state the value is considerably larger although not 0.5.

The reason for these results can be simply understood on the basis of the Fermi surface of the hypothetical Pauli paramagnetic metal of Figure 9b. Metals with nested Fermi surfaces are susceptible to a modulation with wave vector q (i.e., the nesting vector) of their charge or spin density, which destroys the nested parts of the Fermi surface.[33] If the nesting is complete, the modulation thus leads to the destruction of the Fermi surface, and the conductivity becomes activated (i.e., semiconducting). When electron repulsions are important, the spin modulation becomes preferred. Since the two open warped lines of Figure 9b are very well nested by the $q = a^*/2$ wave vector, the AF ground state of the present salts can thus be seen as arising from such nesting mechanism of a hypothetical higher energy metallic state. Whereas the AF and AFb states lead to a partial destruction of the Fermi surface, only the AFa state leads to a complete destruction and thus, to a maximum stabilization. These results suggest that looking for nesting properties of the Fermi surface for the hypothetical metallic state can be a powerful tool in the study of TTF-based magnetic salts.

Bromine versus Iodine Salts. The magnetic susceptibility measurements discussed above show that the iodine salt exhibits an even slightly higher value of the Néel temperature. The electronic structure of this salt is in any respect almost identical to that of the bromine salt. However, we note that the energy difference of the AFa state with respect to the hypothetical metallic state is also slightly larger, suggesting a slightly larger stability of this state for the iodine salt. The calculated magnetic coupling constants of Table 3, suggest that in the iodine salt there is a slight decrease of the AF interactions along the *a* direction that is slightly overcompensated by an increase of those along the $a - b$ direction. The origin of these results can be easily traced back to the subtle variations in interdimer contacts in the two salts reported in Table 2.

We believe that the Néel ordering temperatures of these salts are largely determined by the magnetic interactions within the layer, as discussed for other layered materials like Rb_2CrCl_4, for instance.[34] As shown by the values of Table 3, magnetic ordering is more robust in the chains of dimers along the *a* direction. However, it is only when the order between these chains sets in as a result of the J_{a-b} interactions that the 3D condensation of the AF state occurs, because of the very weak interlayer couplings which are nevertheless sufficient to induce 3D order. Thus, we propose that it is the strength of the interactions along the $a - b$ direction which to a large extent determine the Néel temperature of these layered materials. Consequently, the slight shortening of the interdimer contacts along this direction in the iodine salt are most probably at the origin of the observed increase in the Néel temperature.

CONCLUSIONS

The origin of the strongly stabilized AF ground state of an organic conductor characterized with strong electronic correlations has been rationalized here for the first time on the basis of first-principles band structure calculations and specifically on the basis of the relative energies of the possible ferromagnetic,

dx.doi.org/10.1021/ic2002964 |*Inorg. Chem.* 2011, 50, 4171–4181

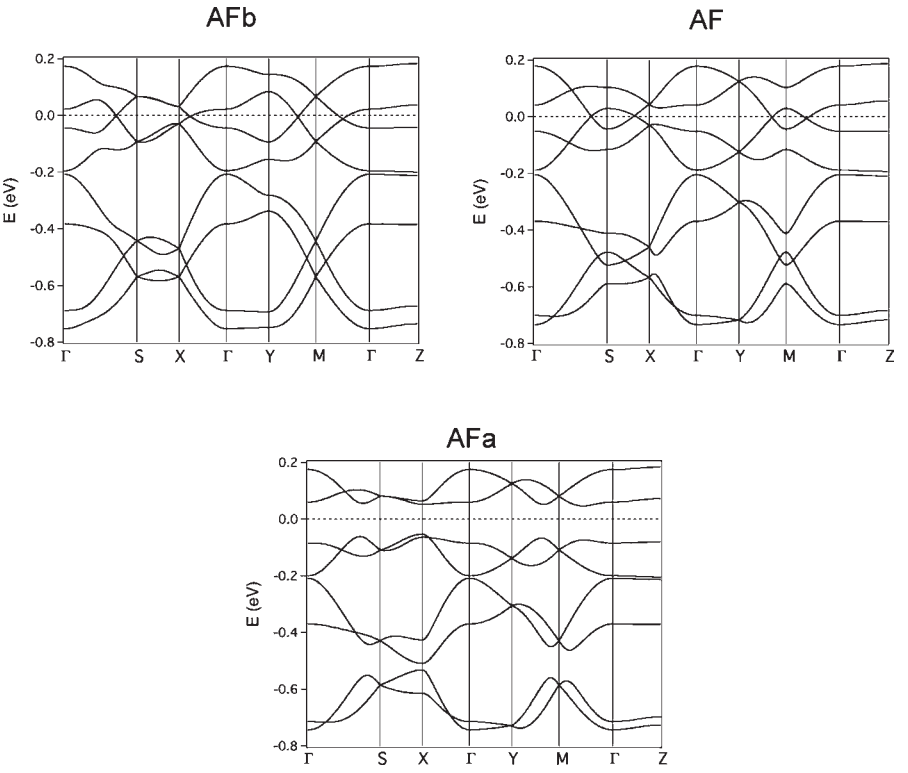

Figure 12. Band structure (HOMO bands) for the calculated AFb, AF, and AFa states of $(tTTF)_2Br$. Actually every band is the superposition of two identical spin-up and spin-down bands. Note that the band structures for AFb and AF do not exhibit a band gap and thus are AF metals. The dashed line in these band structures refers to the Fermi level. The band structure for AFa corresponds to a semiconducting antiferromagnet.

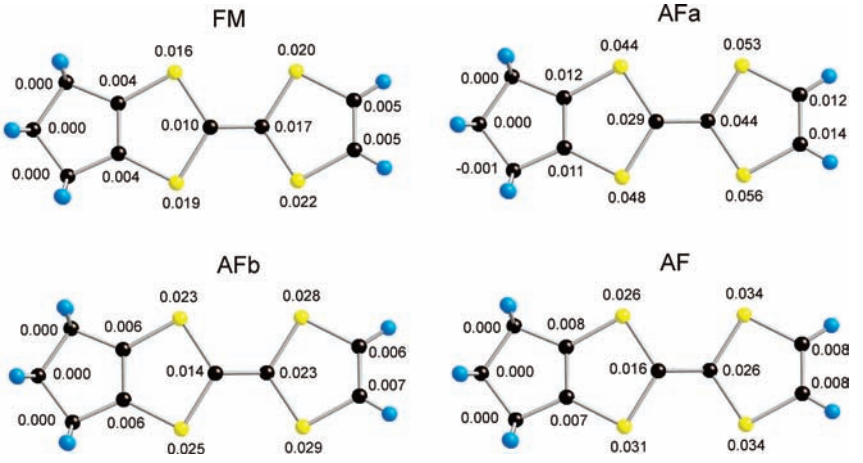

Figure 13. Calculated spin density distribution for the FM, AFa, AFb, and AF states.

metallic and AF phases. These results also suggest that looking for nesting properties of the Fermi surface for the hypothetical metallic state can be a powerful tool in the study of TTF-based insulating salts, providing a very useful way to understand the magnetic structures of these salts.

EXPERIMENTAL SECTION

Synthesis and Crystal Growth. *Synthesis of Carbamate* ***1***. To a suspension of piperidinium piperidinedithiocarbamate (21 g, 85.2 mmol) in refluxing EtOH (160 mL) is added 2-chlorocyclopentanone (10 g, 84 mmol) dropwise. After stirring under reflux for 5 h, the cooled mixture is evaporated, and the orange solid dissolved in CH_2Cl_2 (250 mL). The organic phase is washed with H_2O (3 × 40 mL), dried on $MgSO_4$, and evaporated. Recrystallization from EtOH afforded **1** as white crystals (17.4 g, 85%). Mp 87−88 °C. ^1H RMN ($CDCl_3$, TMS, 300 MHz) δ 1.64 (broad s. 6H); 1.89 (m. 2H); 2.06 (m. 1H); 2.22 (m. 1H); 2.41 (m. 1H); 2.64 (m. 1H); 4.02 (d. Broad 4H); 4.78 (m. 1H). ^{13}C NMR ($CDCl_3$, TMS, 300 MHz) δ 20.6, 24.2, 25.7 (d), 31.3, 37.2, 52.7 (d), 57.2, 193.6, 213.9. Anal. Calcd for $C_{11}H_{17}NOS_2$ (MW 243.3941 g/mol): C, 54.28; H, 7.04; N, 5.75. Found: C, 54.49; H, 6.99; N, 5.74.

Synthesis of Iminium Salt ***2***. To a degassed solution of concentrated H_2SO_4 (95−97%, 40 mL), cooled at 0 °C, is added slowly Et_2O (4 mL), followed by solid **1** (12.4 g, 51 mmol) by fractions. The reaction is then

dx.doi.org/10.1021/ic2002964 |*Inorg. Chem.* 2011, 50, 4171–4181

Table 5. Crystallographic Data for $(tTTF)_2X$ Salts

compound	$(tTTF)_2Cl$	$(tTTF)_2Br$	$(tTTF)_2I$
formula	$C_{18}H_{16}ClS_8$	$C_{18}H_{16}BrS_8$	$C_{18}H_{16}IS_8$
FW ($g\cdot mol^{-1}$)	524.24	568.70	615.68
crystal color	black	black	black
crystal size (mm)	0.41 × 0.09 × 0.08	0.2 × 0.1 × 0.1	0.28× 0.23 × 0.15
crystal system	monoclinic	triclinic	triclinic
space group	$P2_1$	$P\bar{1}$	$P\bar{1}$
T (K)	293(2)	293 (2)	293 (2)
a (Å)	6.3908(4)	6.3441(2)	6.3911(3)
b (Å)	13.9355(5)	7.3344(3)	7.3621(4)
c (Å)	23.4274(6)	12.5028(4)	12.7704(6)
α (deg)	90.00	73.415(3)	73.978(3)
β (deg)	90.623(5)	83.968(2)	85.998(4)
γ (deg)	90.00	72.264(3)	72.096(3)
V ($Å^3$)	2086.30(16)	530.95(3)	549.49(5)
Z	4	1	1
D_{calc} ($g\cdot cm^{-3}$)	1.669	1.779	1.861
μ (mm^{-1})	0.988	2.726	2.221
total refls.	57032	7280	10883
absorption correction	multiscan	multiscan	multiscan
T_{min}, T_{max}	0.899, 0.924	0.728, 0.761	0.547, 0.717
unique refls. (R_{int})	9241 (0.0254)	2436 (0.0232)	2536 (0.0240)
unique refls. ($I > 2\sigma(I)$)	7710	2098	2354
refined param.	487	125	125
R_1 ($I > 2\sigma(I)$)	0.0340	0.0239	0.0191
wR_2 (all data)	0.0742	0.0555	0.0494
goodness-of-fit	1.087	1.081	1.134
residual dens (e^- $Å^{-3}$)	0.28, −0.23	0.22, −0.29	0.28, −0.50

$R_1 = \Sigma||F_o| - |F_c||/\Sigma|F_o|$; $wR_2 = [\Sigma w(F_o^2 - F_c^2)^2/\Sigma wF_o^4]^{1/2}$.

heated slowly to 60 °C and maintained at 60 °C for 2 h. The thick solution is poured slowly on ice (100 g). Addition of HPF_6 (60% wt in H_2O, 18.72 g, 10.7 mL, 77 mmol) leads to the precipitation of the PF_6^- salt. The filtered solid is extracted with CH_2Cl_2, and the combined organic solutions washed with $NaHCO_3$, H_2O, and dried on $MgSO_4$. Recrystallization by dissolution in CH_2Cl_2 and addition of Et_2O afforded the salt **2** as white microcrystals (11.3 g, 60%). Mp 159 °C. ^1H RMN ($CDCl_3$, TMS, 300 MHz) δ 1.82 (m. 2H); 1.91 (m. 4H); 2.55 (quint. 2H); 2.94 (t. 4H); 3.84 (t. 4H). ^{13}C NMR ($CDCl_3$, TMS, 300 MHz) δ 21.7; 24.9; 27.1; 30.8; 56.69; 136.27; 193.01. Anal. Calcd for $C_{11}H_{16}F_6NPS_2$ (MW 371.3509 g/mol): C, 35.58; H, 4.34, N, 3.77. Found C, 35.72; H, 4.14; N, 3.73%.

Trimethylenetetrathiafulvalene (tTTF). To a suspension of 1,3-dithiol-2-ylium iodide (2 g, 8.7 mmol) in freshly distilled MeCN (20 mL) is added trimethylphosphite (1.02 mL, 8.7 mmol). The resulting solution is evaporated (T < 35 °C) and the oily residue is directly dissolved in freshly distilled tetrahydrofuran (THF, 70 mL) and cooled to −70 °C. A suspension of *t*BuOK (0.98 g, 8.7 mmol) in dry THF (18 mL) is added keeping the reaction temperature between −70 °C/−60 °C. 1-(5,6-Dihydro-4*H*-cyclopenta[*d*][1,3]dithiol-2-ylidene)piperidinium hexafluorophosphate (**2**) (3.22 g, 8.7 mmol) is then added, and the temperature is allowed to warm up to −10 °C within 2 h. Anhydrous Et_2O (100 mL) is added, and the white precipitate formed is filtered thought Celite and washed with Et_2O. The combined filtered solutions are concentrated, diluted with degassed toluene (18 mL), followed by dropwise addition of glacial acetic acid (4 mL). After stirring for 30 min, water is added to the dark red solution, and the mixture is extracted with CH_2Cl_2, the organic phase is washed with a sodium metabisulfite solution (20% in water), and dried over $MgSO_4$. The product is purified on a short chromatographic column (SiO_2/CH_2Cl_2) and recrystallized from MeCN to yield tTTF as yellow crystals (0.98 g, 46%). Mp: 142 °C (litt.[11d] 141 °C). ^1H NMR ($CDCl_3$, TMS): δ 2.34 (m); 2.45 (broad s.); 6.22 (s). ^{13}C NMR ($CDCl_3$, TMS): δ 27.64; 30.17; 111.25; 119.63; 118.82; 133.14. Elem. Anal. Calcd. for $C_9H_8S_4$ (MW = 244.4265 g/mol): C, 44.23; H, 3.30. Found: C, 44.41; H, 3.21%. Cyclic voltammetry (CH_2Cl_2/*n*-Bu_4NPF_6 0.2 M, in V vs SCE): E°_1 = 0.33, E°_2 = 0.83 V.

$(tTTF)_2X$ Salts. Crystal growth was performed by electrocrystallization[35] in two-compartment cells with Pt electrodes (diameter 1 mm, length 2 cm). Solutions of 0.1 M *n*Bu_4NX (X = Cl, Br, I) in dry EtOH were used as electrolyte with 10 mg tTTF in the anodic compartment. Current of 1 μA was applied. Crystals grown on the electrode were collected after 1 week, rinsed with EtOH, and dried in air. Alternatively, the iodide salt was also obtained by diffusion technique using a U-shaped cell with a solution of tTTF (10 mg) in CH_2Cl_2 (10 mL) at the bottom of the cell, with a solution of *n*Bu_4NI_3 (0.1 M) in CH_3CN (10 mL) above in both arms of the U tube. Black crystals precipitated at the bottom of the tube after a few days.

X-ray Diffraction Studies. Single crystals were mounted on the top of a thin glass fiber. Data were collected on a Nonius KappaCCD Diffractometer at room temperature with graphite-monochromated Mo−Kα radiation (λ = 0.71073 Å). Structures were solved by direct methods (SHELXS-97) and refined (SHELXL-97)[36] by full-matrix least-squares methods, as implemented in the WinGX software package.[37] Absorption corrections were applied. Hydrogen atoms were introduced at calculated positions (riding model), included in structure factor

dx.doi.org/10.1021/ic2002964 |*Inorg. Chem.* 2011, 50, 4171–4181

calculations, and not refined. Crystallographic data of both salts are summarized in Table 5.

Resistivity Measurements. To measure the longitudinal resistivity, gold pads were evaporated on the surface of the crystals to improve the quality of the contacts. Then a standard four points technique was used with a low frequency lock-in detection ($I_{ac} = 0.1-1\ \mu A$). High hydrostatic pressure was provided by a NiCrAl clamped cell up to 25 kbar, using silicon oil (Daphne 7373) as the pressure transmitting medium. The pressures at room temperature were deduced from the resistance of a manganin gauge located close to the sample in the pressure cell. While applying pressure, the resistance of the sample and the resistance of the manganin wire are measured as a function of time, and the data points on Figure 6 correspond to time intervals of 10 s. The pressures at low temperature are indicated on the figures, taking into account the loss of pressure during cooling which is estimated to 2 kbar. The temperature is measured in the pressure cell with a Copper-Constantan thermocouple. Low temperatures have been provided by a cryocooler equipment down to 25 K.

Magnetic Measurements. The magnetic susceptibility measurements were obtained with the use of a Quantum Design SQUID magnetometer MPMS-XL. This magnetometer works between 1.8 and 400 K for direct current (dc) applied fields ranging from −5 to 5 T. Measurements were performed on polycrystalline samples of $(tTTF)_2Br$ (30.8 mg, obtained from multiple electrocrystallization cells) and $(tTTF)_2I$ (11.1 mg, obtained from chemical oxidation with nBu_4NI_3). The magnetic data were corrected for the sample holder and the diamagnetic contributions. Low field data determined in the low temperature regime (see Figure 8) were translated to the reference susceptibility value measured at 50 kG.

Electronic Structure Calculations. First-principles spin-polarized calculations were carried out using a numerical atomic orbitals DFT approach[38] developed for efficient calculations in large systems and implemented in the SIESTA code.[39−41] We have used the generalized gradient approximation (GGA) to DFT and, in particular, the functional of Perdew, Burke, and Ernzerhof.[42] Only the valence electrons are considered in the calculation, with the core being replaced by norm-conserving scalar relativistic pseudopotentials[43] factorized in the Kleinman−Bylander form.[44] We have used a split-valence double-ζ basis set including polarization orbitals as obtained with an energy shift of 10 meV for all atoms.[45] The energy cutoff of the real space integration mesh was 250 Ry, and the Brillouin zone was sampled using grids of $(3 \times 2 \times 3)$ *k*-points.[46]

The DFT spin-polarized calculations for discrete dimeric units were carried out adopting the hybrid B3LYP functional,[47] which has given excellent results for the calculation of magnetic coupling constants for a large variety of molecular systems.[48] A basis set of double-ζ quality[49] was used. The calculations were carried out using the Gaussian 03 code.[50] The geometries were the same employed for the periodic calculations. The coupling constants were calculated according to the procedure described by Ruiz, Cano, Álvarez, and Alemany.[51]

■ ASSOCIATED CONTENT

Supporting Information. Crystallographic data in CIF format. Further details are given in Figures S1 and S2. This material is available free of charge via the Internet at http://pubs.acs.org.

■ AUTHOR INFORMATION

Corresponding Author

*E-mail: marc.fourmigue@univ-rennes1.fr (M.F.); p.alemany@ub.edu (P.A.); canadell@icmab.es (E.C.).

■ ACKNOWLEDGMENT

This work was supported by DGI-Spain (Grants CSD2007-00041, FIS2009-12721-C04-03, CTQ2008-06670-C02-02/BQU, and CTQ2008-06549-C02-01/BQU), Generalitat de Catalunya (2009 SGR 1459 and 2009 SGR 462), XRQTC and by grants for computer time from CESCA. Financial support from French government (Postdoctoral grant to E.W.R.) and the ANR-France (Grant ANR-08-BLAN-0140-2) is also gratefully acknowledged. A.R.-F. acknowledges support through the Ramón y Cajal program (DGI-Spain). We thank Thierry Guizouarn (Centre de Mesures Physiques, Rennes) for magnetic measurements and Thierry Roisnel at CDIFX (Rennes) for access to X-ray diffractometers.

■ REFERENCES

(1) Enoki, T.; Miyazaki, A. *Chem. Rev.* **2004**, *104*, 5449.
(2) (a) Fabre, J.-M.; Galaine, C.; Giral, L.; Chasseau, D. *Tetrahedron Lett.* **1982**, *23*, 1813. (b) Tatemitsu, H.; Nishikawa, E.; Sakata, Y.; Misumi, S. *Synth. Met.* **1987**, *19*, 565.
(3) Chasseau, D.; Gaultier, J.; Miane, J. L.; Coulon, C.; Delhaes, P.; S. Flandrois, S.; Fabre, J.-M.; Giral, L. *J. Phys. (Paris)* **1983**, *44*, 1223.
(4) Vaca, P.; Coulon, C.; Ravy, S.; Pouget, J. P.; Fabre, J.-M. *J. Phys. I* **1991**, *1*, 125.
(5) (a) Fabre, J.-M.; Gouasmia, A. K.; Giral, L.; Gaultier, M. *New J. Chem.* **1988**, *12*, 119. (b) Chasseau, D.; Gaultier, J.; Hauw, C.; Fabre, J.-M.; Giral, L.; Torreilles, E. *Acta Crystallogr., Sect. B* **1978**, *34*, 2811.
(6) Ishibashi, S.; Kohyama, M. *Phys. Rev. B* **2000**, *62*, 7839.
(7) Sing, M.; Claessen, R.; Finteis, Th.; Hao, S.; Hüfner, S.; Blaha, P. *J. Electron Spectrosc. Relat. Phenom.* **2001**, *114−116*, 717.
(8) Rovira, C.; Novoa, J. J.; Mozos, J. L.; Ordejón, P.; Canadell, E. *Phys. Rev. B* **2002**, *65*, 081104.
(9) Lee, Y. J.; Nieminen, R. M.; Ordejón, P.; Canadell, E. *Phys. Rev. B* **2003**, *67*, 180505(R).
(10) Fraxedas, J.; Lee, Y. J.; Jiménez, J.; Gago, R.; Nieminen, R. M.; Ordejón, P.; Canadell, E. *Phys. Rev. B* **2003**, *68*, 195115.
(11) Ishibashi, S. *Sci. Technol. Adv. Mater.* **2009**, *10*, 024311.
(12) Llusar, R.; Vicent, C.; Uriel, S.; Clemente-Juan, J. M.; Coronado, E.; Gómez-García, C.; Braïda, B.; Canadell, E. *J. Am. Chem. Soc.* **2004**, *126*, 12076.
(13) Ishibashi, S.; Terakura, K.; Kobayashi, A. *J. Phys. Soc. Jpn.* **2008**, *77*, 024702.
(14) Ishibashi, S.; Tanaka, H.; Kohyama, M.; Tokumoto, M.; Kobayashi, A.; Kobayashi, H.; Terakura, K. *J. Phys. Soc. Jpn.* **2005**, *74*, 843.
(15) Tenn, N.; Bellec, N.; Jeannin, O.; Piekara-Sady, L.; Auban-Senzier, P.; Íñiguez, J.; Canadell, E.; Lorcy, D. *J. Am. Chem. Soc.* **2009**, *131*, 16961.
(16) Fabre, J.-M. *Chem. Rev.* **2004**, *104*, 5133.
(17) (a) Fabre, J.-M.; Toreilles, E.; Gibert, J. P.; Chanaa, M.; Giral, L. *Tetrahedron Lett.* **1977**, *46*, 4033. (b) Fabre, J.-M.; Galaine, C.; Giral, L. *J. Phys., Coll.* **1983**, 1153–8.
(18) Gonnella, C.; Cava, M. P. *J. Org. Chem.* **1978**, *43*, 369.
(19) (a) Fabre, J.-M.; Galaine, C.; Giral, L.; Chasseau, D. *Tetrahedron Lett.* **1982**, *23*, 1813. (b) Giral, L.; Fabre, J.-M.; Gouasmia, A. *Tetrahedron Lett.* **1986**, *27*, 4315. (c) Fabre, J.-M.; Giral, L.; Gouasmia, A.; Cristau, H.-J.; Ribeill, Y. *Bull. Soc. Chim. Fr.* **1987**, *5*, 823. (d) Fabre, J.-M.; Gouasmia, A.; Giral, L.; Galtier, M. *New. J. Chem.* **1988**, *12*, 119.
(20) Fourmigué, M.; Batail, P. *Bull. Soc. Chim. Fr.* **1992**, *129*, 29. (b) Fourmigué, M.; Huang, Y.-S. *Organometallics* **1993**, *12*, 797. (c) Fourmigué, M.; Krebs, F. C.; Larsen, J. *Synthesis* **1993**, 509. (d) Gerson, F.; Lamprecht, A.; Fourmigué, M. *J. Chem. Soc., Perkin Trans. II* **1996**, 1409. (e) Fourmigué, M.; Mézière, C.; Canadell, E.; Zitoun, D.; Bechgaard, K.; Auban-Senzier, P. *Adv. Mater.* **1999**, *11*, 766.
(21) Fourmigué, M.; Reinheimer, E. W.; Dunbar, K, R.; Auban-Senzier, P.; Pasquier, C.; Coulon, C. *J. Chem. Soc., Dalton Trans.* **2008**, 4652.
(22) Lerstrup, K.; Johannsen, I.; Jorgensen, M. *Synth. Met.* **1988**, *27*, B9.
(23) Desiraju, G. R.; Steiner, T. *The Weak Hydrogen Bond*; Oxford University Press: Oxford, NY, 1991; Aakeröy, C. B.; Evans, T. A.; Seddon, K. R.; Palinko, I. *New. J. Chem.* **1999**, *23*, 145.

(24) Fourmigué, M.; Batail, P. *Chem. Rev.* **2004**, *104*, 5379.
(25) Batail, P.; LaPlaca, S. J.; Mayerle, J. J.; Torrance, J. B. *J. Am. Chem. Soc.* **1981**, *103*, 951.
(26) Whangbo, M.-H.; Williams, J. M.; Schultz, A. J.; Emge, T. J.; Beno, M. A. *J. Am. Chem. Soc.* **1987**, *109*, 90. Novoa, J. J.; Mota, F.; Whangbo, M.-H.; Williams, J. M. *Inorg. Chem.* **1991**, *30*, 54.
(27) Dautel, O. J.; Fourmigué, M.; Canadell, E. *Chem.—Eur. J.* **2001**, *7*, 2635.
(28) Steiner, T. *New J. Chem.* **1998**, *23*, 1099.
(29) Bechgaard, K.; Jacobsen, C.; Mortensen, K.; Pedersen, H.; Thorup, N. *Solid State Commun.* **1979**, *33*, 1119.
(30) Bonner, J. C.; Fisher, M. E. *Phys. Rev. A* **1964**, *135*, 640.
(31) (a) Kahn, O. *Molecular Magnetism*; VCH: New York, 1993; Chapter 11, pp 251−286; (b) Estes, W.; Gavel, D. P.; W.E. Hatfield, W. E.; Hogdson, D. *Inorg. Chem.* **1978**, *17*, 1415.
(32) Note that because of the itinerant component in several states (which varies for different solutions) it is not possible to calculate the magnetic coupling constants from the energy differences of appropriate spin configurations of the solid.
(33) Canadell, E.; Whangbo, M.-H. *Chem. Rev.* **1991**, *91*, 965.
(34) Bramwell, S. T.; Holdsworth, P. C. W.; Hutchings, M. T. *J. Phys. Soc. Jpn.* **1995**, *64*, 3066.
(35) Batail, P.; Boubekeur, K.; Fourmigué, M.; Gabriel, J.-C. P. *Chem. Mater.* **1998**, *10*, 3005.
(36) Sheldrick, G. M.; *SHELX97 - Programs for Crystal Structure Analysis*, Release 97-2; Bruker AXS: Madison, WI, 1998.
(37) Farrugia, L. J. *J. Appl. Crystallogr.* **1999**, *32*, 837.
(38) Hohenberg, P.; Kohn, W. *Phys. Rev.* **1964**, *136*, B864. Kohn, W.; Sham, L. J. *Phys. Rev.* **1965**, *140*, A1133.
(39) Soler, J. M.; Artacho, E.; Gale, J. D.; García, A.; Junquera, J.; Ordejón, P.; Sánchez-Portal, D. *J. Phys.: Condens. Matter.* **2002**, *14*, 2745.
(40) For more information on the SIESTA code visit: http://www.uam.es/siesta/
(41) For a review on applications of the SIESTA approach in materials science see: Sánchez-Portal, D.; Ordejón, P.; Canadell, E. *Struct. Bonding (Berlin)* **2004**, *113*, 103.
(42) Perdew, J. P.; Burke, K.; Ernzerhof, M. *Phys. Rev. Lett.* **1996**, *77*, 3865.
(43) Troullier, N.; Martins, J. L. *Phys. Rev. B* **1991**, *43*, 1993.
(44) Kleinman, L.; Bylander, D. M. *Phys. Rev. Lett.* **1982**, *48*, 1425.
(45) Artacho, E.; Sánchez-Portal, D.; Ordejón, P.; García, A.; Soler, J. M. *Phys. Status Solidi B* **1999**, *215*, 809.
(46) Monkhorst, H. J.; Pack, J. D. *Phys. Rev. B* **1976**, *13*, 5188.
(47) Becke, A. D. *J. Chem. Phys.* **1993**, *98*, 5648.
(48) Ruiz, E. *Struct. Bonding (Berlin)* **2004**, *113*, 71. Ruiz, E.; Alemany, P.; Alvarez, S.; Cano, J. *J. Am. Chem. Soc.* **1997**, *119*, 1297.
(49) Schaefer, A.; Huber, C.; Ahlrichs, R. *J. Chem. Phys.* **1994**, *100*, 5829.
(50) Frisch, M. J.; Trucks, G. W.; Schlegel, H. B.; Scuseria, G. E.; Robb, M. A.; Cheeseman, J. R.; Montgomery Jr., J. A.; Vreven, T.; Kudin, K. N.; Burant, J. C.; Millam, J. M.; Iyengar, S. S.; Tomasi, J.; Barone, V.; Mennucci, B.; Cossi, M.; Scalmani, G.; Rega, N.; Petersson, G. A.; Nakatsuji, H.; Hada, M.; Ehara, M.; Toyota, K.; Fukuda, R.; Hasegawa, J.; Ishida, M.; Nakajima, T.; Honda, Y.; Kitao, O.; Nakai, H.; Klene, M.; Li, X.; Knox, J. E.; Hratchian, H. P.; Cross, J. B.; Bakken, V.; Adamo, C.; Jaramillo, J.; Gomperts, R.; Stratmann, R. E.; Yazyev, O.; Austin, A. J.; Cammi, R.; Pomelli, C.; Ochterski, J. W.; Ayala, P. Y.; Morokuma, K.; Voth, G. A.; Salvador, P.; Dannenberg, J. J.; Zakrzewski, V. G.; Dapprich, S.; Daniels, A. D.; Strain, M. C.; Farkas, O.; Malick, D. K.; Rabuck, A. D.; Raghavachari, K.; Foresman, J. B.; Ortiz, J. V.; Cui, Q.; Baboul, A. G.; Clifford, S.; Cioslowski, J.; Stefanov, B. B.; Liu, G.; Liashenko, A.; Piskorz, P.; Komaromi, I.; Martin, R. L.; Fox, D. J.; Keith, T.; Al-Laham, M. A.; Peng, C. Y.; Nanayakkara, A.; Challacombe, M.; Gill, P. M. W.; Johnson, B.; Chen, W.; Wong, M. W.; Gonzalez, C.; Pople, J. A. *Gaussian 03*, Revision C.02; Gaussian, Inc.: Wallingford, CT, 2004.
(51) Ruiz, E.; Cano, J.; Alvarez, S.; Alemany, P. *J. Comput. Chem.* **1999**, *20*, 1391.